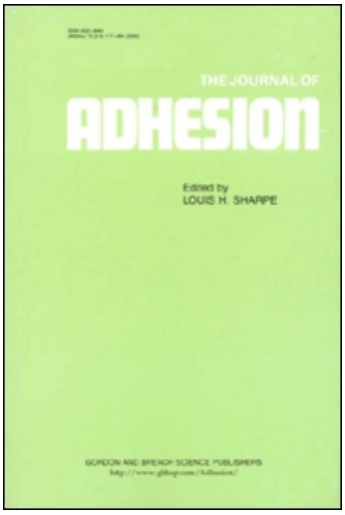

The Journal of Adhesion
Publication details, including instructions for authors and subscription information:
http://www.informaworld.com/smpp/title~content=t713453635

Hydrothermal Aging of Composite Materials Part 1 : Interfacial Aspects

D. H. Kaelble[a]; P. J. Dynes[a]; L. Maus[b]
[a] Science Center. Rockwell International, Thousand Oaks, California, U.S.A. [b] Tulsa Division, Rockwell International,

To cite this Article Kaelble, D. H. , Dynes, P. J. and Maus, L.(1976) 'Hydrothermal Aging of Composite Materials Part 1 : Interfacial Aspects', The Journal of Adhesion, 8: 2, 121 — 144
To link to this Article: DOI: 10.1080/00218467608075078
URL: http://dx.doi.org/10.1080/00218467608075078

J. Adhesion, 1976, Vol. 8, pp. 121–144

Printed in Scotland

Hydrothermal Aging of Composite Materials

Part 1 : Interfacial Aspects

D. H. KAELBLE, P. J. DYNES

Science Center, Rockwell International, Thousand Oaks, California 91360, U.S.A.

and

L. MAUS

Tulsa Division, Rockwell International

(*Received December 15, 1975*)

A surface energetics theory of bonded interfaces is applied to design graphite–epoxy composites with controlled moisture sensitivity at the fiber-matrix interface. Hydrothermal (100°C in H_2O), aging of the composite materials shows an equilibrium degree of degradation in interlaminar shear strength λ_b which is in reasonable agreement with theoretical expectation. Hydrothermal aging produces changes in composite acoustic response, both sound velocity C_2 and attenuation α_2, which correlate with changes in λ_b or reduced aging time t/τ where τ is the relaxation time for hydrothermal degradation. The temperature dependence of λ_b is also shown to be modified by hydrothermal aging indicating possible changes in the chemical structure and rheology of the cured epoxy matrix phase.

INTRODUCTION

A series of recent reports have developed and extensively applied both surface energetics and micro-mechanics models to analyze the property degradation effects of high moisture exposure on graphite–epoxy composites.[1-4] These studies have shown a close correlation between analytical predictions and experimentally observed changes in interlaminar and translaminar shear strength and transfibrous fracture energy in uniaxially reinforced composites. Prior to moisture degradation the composite specimen exhibit high inter- and translaminar shear strength $\lambda_b \geqslant 850$ kg/cm^2 (12,000 psi) and relatively low

transfibrous fracture energy $W_b/A \simeq 10-20$ kg cm/cm^2 (56–112 lb. in/in^2). Exposure to 90% relative humidity or water immersion at 100°C for times $t \geqslant 7.2 \cdot 10^5$ sec (200 hr) produces a 30 to 50% reduction in λ_b accompanied by a two to five fold increase in W_b/A.[4] These property changes are shown to be irreversible and directly related to cumulative moisture degradation of the fiber matrix interfacial bond.

These recent analytic and experimental results confirm published reports[5-7] which show that exposure of graphite–epoxy or graphite–polyester composites to water immersion or water vapor at elevated temperature produces decreased interlaminar shear strength accompanied by rising or falling values of transfibrous fracture toughness. The designation of failure modes discussed here follows the definitions of Cook and Downhill[8] as illustrated in Figure 1.

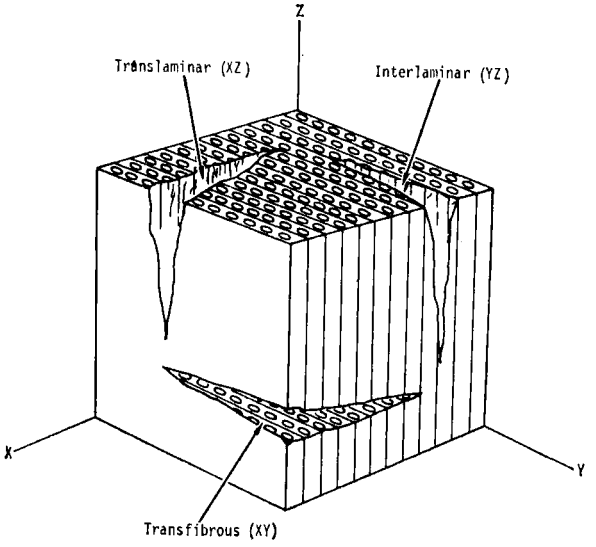

FIGURE 1 Definition of cracks (from Ref. 8).

An approach to the correction of this moisture sensitivity in graphite reinforced composites has been suggested by Kaelble and co-workers[9-11] wherein fiber surface treatment would be directed to producing high values of (London-d) dispersion γ_{sv}^d and low (Keesom-p) polar γ_{sv}^p contribution to fiber solid–vapor surface tension $\gamma_{sv} = \gamma_{sv}^d + \gamma_{sv}^p$. Selection of matrix materials with complimentary high γ^d and low γ^p surface properties and nonpolar bulk (solubility) properties is expected to produce both a moisture insensitive interfacial and rheological response in the reinforced composite. [10]

This discussion details the results of a study in which the fiber matrix

interface in graphite–epoxy composite is both stabilized and sensitized to moisture degradation by fiber surface treatment. The first objective of the study is to test predictions from surface energetics models with regard to the equilibrium values of moisture degradation as related to surface property studies. The second objective is to determine whether moisture sensitization

TABLE I

Symbols and nomenclature

Surface energetics failure criteria

σ_c = Critical crack propagation stress
γ_G = Griffith surface energy for fracture
E = Young's modulus
C = Crack length
α, β = respective square-root of the (London-d) dispersion γ^d and (Keesom-p) polar γ^p parts of liquid-vapor $\gamma_{LV} = \gamma^d_{LV} + \gamma^p_{LV}$ or solid-vapor $\gamma_{sv} = \gamma^d_{sv} = \gamma^p_{sv}$ surface tension
α_1, β_1 = surface properties of matrix
α_2, β_2 = surface properties of immersion phase
α_3, β_3 = surface properties of fiber

Kinetic criteria for cumulative damage

ϕ = fractional degree of degradation
$\lambda_{b0}, \lambda_{b\infty}$ = interlaminar shear strength at $t = 0$ at $t = \infty$
t = hydrothermal exposure time
t_i = initiation time for hydrothermal degradation
b = time exponent for degradation
a_T, a_M, a_C = dimensionless time shift factors relating to thermal (T), mechanical (M) and environmental (C) stress effects
K = system constant

Microstructure factors

r_0 = fiber radius
a = fiber–fiber separation distance
V = fiber volume fraction (hexagonal packing)

Physical conversions

dyn cm^{-1} = erg cm^{-2} = 10^{-3} JM^{-2}
kg cm^{-2} = 9.81 . 10^4 Nm^{-2} = 14.2 psi

modifies the kinetics of cumulative degradation shear bond strength at the fiber-matrix interface. Additional experiments were included to detail changes in ultrasonic energy absorption and temperature dependence of shear strength due to high moisture aging. The symbols and nomenclature for the principal parameters which define the scope of this discussion are presented in Table I.

THEORY

A surface energetics model for describing the critical stress for crack propagation σ_c in terms of the reversible part of the Griffith fracture energy γ_G has recently been developed which provides the following relations[11]:

$$\gamma_G = R^2 - R_0^2 \tag{1}$$

$$R_0^2 = \tfrac{1}{4}(\alpha_1 - \alpha_3)^2 + (\beta_1 - \beta_3)^2 \tag{2}$$

$$R^2 = (\alpha_2 - H)^2 + (\beta_2 - K)^2 \tag{3}$$

$$H = \tfrac{1}{2}(\alpha_1 + \alpha_3) \tag{4}$$

$$K = \tfrac{1}{2}(\beta_1 + \beta_3) \tag{5}$$

$$\sigma_c = \left(\frac{2E\gamma_G}{\pi C}\right)^{\frac{1}{2}} = \left(\frac{2E}{\pi C}\right)^{\frac{1}{2}} (R^2 - R_0^2)^{\frac{1}{2}} \geqslant 0 \tag{6}$$

The physical parameters of Eqs. 1–6 are summarized in Table I. Inspection of Eqs. 1–6 indicates that the modified Griffith expression of Eq. 1 can be conveniently represented on cartesian coordinates of α *versus* β. The point H, K defined by Eq. 4 and Eq. 5 defines the origin of a cylindrical coordinate system wherein $\sigma_c = 0$ if $R \leqslant R_0$. The vectors R (air) and R (H_2O) originate at H, K and terminate at the surface properties of the immersion phase where for air immersion $\alpha_2 = \beta_2 = 0$ while for water $\alpha_2 = 4.67$ (dyn/cm)$^{\frac{1}{2}}$ and $\beta_2 = 7.14$ (dyn/cm)$^{\frac{1}{2}}$.

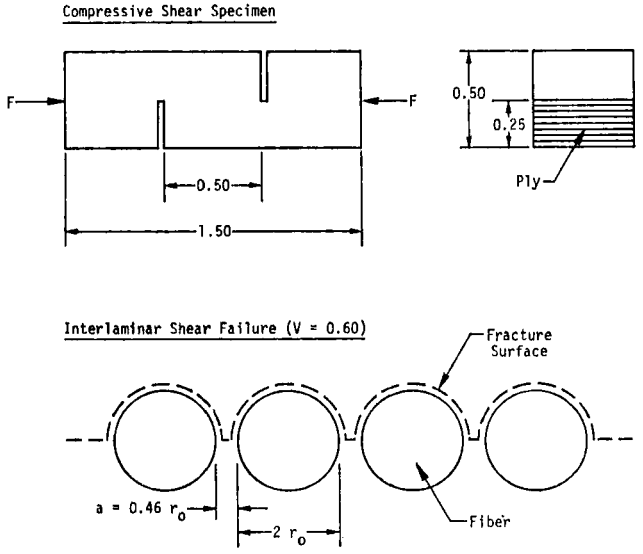

FIGURE 2 Test specimen (upper view) and locus of failure (lower view) for interlaminar shear strength.

Calculation of the relative magnitudes of interlaminar shear strength under equilibrium immersion conditions in air and water require additional consideration of the locus of microfracture in the fiber reinforced composite. For fibers of uniform radius r_0 in regular hexagonal packing the matrix distance a separating adjacent fibers is defined by the following expression[4]:

$$a = r_0(1.074(\pi/V)^{\frac{1}{2}} - 2) \tag{7}$$

applying the geometric model for interlaminar shear failure shown in Figure 2 the fractional areas of interfacial f_I and matrix f_M failure are given by the following relation[4]

$$f_I = 1 - f_M = \frac{\pi r_0}{\pi r_0 + a} \tag{8}$$

The composite interlaminar shear strength λ_b is derived from interfacial λ_I and matrix λ_M failure stresses by the rule of mixtures:

$$\lambda_b = f_I\lambda_I + f_M\lambda_M \tag{9}$$

A properly bonded composite under air immersion should display:

$$\lambda_b = \lambda_{I0} = \lambda_{M0} \tag{10}$$

where the zero suffix denotes zero exposure time $t = 0$ to water immersion. After infinite, $t = \infty$, time exposure to water immersion we further assume that:

$$\lambda_{M\infty} = \lambda_{M0} \tag{11}$$

$$\lambda_I = \lambda_{I0}\frac{\sigma_c(H_2O)}{\sigma_c(\text{air})} \tag{12}$$

Substituting Eq. 10 through Eq. 12 into Eq. 9 we obtain the following relation[4]:

$$r = \frac{\lambda_{b\infty}}{\lambda_{b0}} = (1 - f_I) + f_I\frac{\sigma_c(H_2O)}{\sigma_c(\text{air})} \tag{13}$$

The ratio r of final $t = \infty$ to initial $t = 0$ shear strength can be calculated by Eq. 13. Since the arguments introduced into Eq. 13 are based on equilibrium considerations no information is provided concerning the kinetics of moisture degradation.

A finite exposure time is generally required to establish equilibrium between a composite material response and the environment to which it is exposed. A general procedure for expressing the kinetics of cumulative damage effects due to mechanical (M), thermal (T) or environmental (C = chemical or corrosive) stresses has been proposed by Halpin and coworkers in the following relation[12, 13]

$$\phi = \exp\left[-K(t - t_i)^b/a_T a_M a_C\right] \tag{14}$$

A specialized form of Eq. 14 applicable to analysis of shear strength degradation states[4]:

$$\phi = \frac{\lambda_b(t) - \lambda_{b0}}{\lambda_{b0} - \lambda_{b\infty}} = \exp(-t/\tau) \tag{15}$$

where it is assumed that $b = 1.0$, $t_i = 0$ and the relaxation time $\tau = a_T a_M a_C / K$. Rearranging Eq. 15 we define the interlaminar shear strength $\lambda_b(t)$ at exposure time t by the following expressions[4]:

$$\lambda_b(t) = \lambda_{b\infty} + (\lambda_{b0} - \lambda_{b\infty}) \exp(-t/\tau)] \tag{16}$$

$$\lambda_b(t) = \lambda_{b0} [r + (1-r) \exp(-t/\tau)] \tag{17}$$

The dimensionless strength ratio $r = \lambda_{b\infty}/\lambda_{b0}$ of Eq. 17 isolates the chemical (or thermodynamic) aspect of moisture sensitivity since λ_{b0} is the equilibrium shear strength in air immersion (high moisture aging time = 0) and $\lambda_{b\infty}$ is the shear strength in equilibrium with water ($t = \infty$). The optimized surface energetics approach for chemically modifying the interface toward moisture degradation should provide $r = 1.0$ in Eq. 17 so that from thermodynamic balances of interfacial tensions the shear strengths $\lambda_b(t) = \lambda_{b0} = \lambda_b$ become independent both to time and intensity of high moisture exposure. A second kinetic approach to environmental protection from moisture is identified through the relaxation time τ of Eq. 17. In principle, external barrier coatings can be applied to lower the diffusion rate of water into the composite material and thereby increase the relaxation time for moisture degradation so that $t \ll \tau$ over the service life of the part. Inspection of Eq. 17 shows that for $t/\tau \ll 1.0$ the term $\exp(-t/\tau) \simeq 1.0$ and $\lambda_b(t) = \lambda_{b0}$ independently of $r = \lambda_b/\lambda_{b0}$. The success of this second approach depends entirely upon the resistance of the barrier coating to damage or degradation.

EXPERIMENTAL

This study analyzes the significance of independently adjusting surface properties and $r = \lambda_{b\infty}/\lambda_{b0}$ by varied fiber surface treatment and examining other physical responses including the relaxation time τ for degradation as dependent variables. The graphite fiber chosen as reinforcement was HERCULES HTS® which is supplied as a twist-free tow containing $\simeq$10,000 continuous filaments. This fiber is prepared from a polyacrylonitrile (PAN) precursor and surface treated by the manufacturer to increase interlaminar shear strength.

Previous studies have shown that the producer surface treatments of HTS graphite fibers display a highly polar surface character where $\tau_{sv}^p/\tau_{sv} \simeq 0.50$ and pronounced susceptibility to moisture degradation. A special study of surface treatments for graphite revealed that chemically reducing heat

treatment in H_2 substantially reduced the polar surface character of fiber surface tension as indicated in Table II for virgin (producer treated) and various H_2 treated fibers which utilized heating at 1000°C for one hour in a flowing 50/50 mixture of hydrogen and argon. In the present study the HTS graphite fiber tow was specially wrapped on carbon spools to permit free circulation of a flowing 90 : 10 mixture of hydrogen : nitrogen at 1038°C for 2 hours. Six sets of fiber samples were taken from the outer and inner wraps of the three rolls exposed for H_2 treatment and analyzed for solid–vapor surface tension properties by methods which duplicate those detailed in previous reports (Ref. 10). The lower portion of Table II summarizes the average values for γ_{sv}^d, γ_{sv}^p, γ_{sv} and the respective standard deviations $\pm\delta^d$,

TABLE II

Surface properties of treated graphite HTS fibers and cured epoxy matrix at 23±1°C and 40±5% R.H.

	$\gamma_{sv}^d \pm \delta^d$ dyn/cm	$\gamma_{sv}^p \pm \delta^p$	$\gamma_{sv} \pm \delta$
Virgin Fiber[10]	25.9±1.5	25.7±3.3	51.6±2.3
Previous H_2 treated[10]	41.1+6.7	12.5±2.7	53.7±6.0
Present H_2 treated			
1) Outer Roll 1	37.9±2.6	10.6+1.4	48.5±1.6
2) Inner Roll 1	38.6±5.7	18.2±3.6	56.8±4.1
3) Outer Roll 2	36.6±2.6	13.4±1.6	50.0±1.5
4) Inner Roll 2	37.6±2.7	12.3±1.6	49.9±1.7
5) Outer Roll 3	40.7±3.9	9.8±1.8	50.5±2.7
6) Inner Roll 3	41.7±6.1	12.3±2.7	53.9±4.7
Average:	38.8±2.0	12.8±3.0	51.6+3.1
Gantrez 169 treated fiber (estimated)	≃21.8	≃51.0	≃72.8
Bloomingdale BP-907® modified epoxy (cured under dry N_2)	37.2±3.1	8.3±2.0	45.5±1.2

$\pm\delta^p$, $\pm\delta$ deduced from fiber wettability measurement and surface energy analysis for the six fiber samples. Inspection of the data in Table II indicates that large scale H_2 treatment of graphite fibers produced in the present study results in surface properties which appear relatively uniform for different sampling positions. The average values of the present and previous H_2 treated graphite fibers agree within the limits of the standard deviations from the mean values with respect to both γ_{sv}^d and γ_{sv}^p.

A second fiber surface treatment was applied to HTS graphite fiber to produce high moisture sensitivity in the composite. In this treatment a 1% (by weight) solution of Gantrez 169 (General Aniline & Film Corp) in methyl ethyl ketone was applied to the fiber tow and dried on the fiber surface.

Gantrez 169 is a high molecular weight copolymer of maleic anhydride and methyl vinyl ether which is highly hydrophilic and water soluble. Fibers resulting from this treatment display water soluble surface properties when tested for wettability by the micro-Wilhelmy plate test method.[3] These surfaces are therefore assigned nominal surface tension values $\gamma_{sv} \simeq 21.8$, $\gamma_{sv}^{p} \simeq 51.0$ (dyn/cm) characteristic of surface hydration by bulk water.

The epoxy resin system BP 907 (Bloomingdale Division of American Cyanamide) has been characterized in earlier studies[4] and the surface properties of this resin are summarized in Table II. Relevant mechanical properties of fiber and matrix materials are summarized in Table III. Uni-

TABLE III

Mechanical properties of components in graphite–epoxy laminates at 23±1°C

Material	Shear modulus G (kg/cm²)	Tensile modulus E (kg/cm²)	Tensile strength σ_b (kg/cm²)
Hercules HTS (diam. = 8.9±0.4 μm)	--	(2.53±0.28) . 10^6	(2.46±0.35) . 10^4
BP907 epoxy (cured)	≃1.19 . 10^4	≃3.16 . 10^4	--

TABLE IV

Constituents and volume fractions of components in uniaxially reinforced graphite–epoxy panels

Reinforced composite panel	SC–2–2 Moisture sensitive	SC–2–3 Moisture resistant
Fiber plys/cm	52	52
Fiber	HTS with Gantrez 169 size[a]	HTS with hydrogen surface treatment[b]
Resin	BP907	BP907
Volume fractions		
Fiber (%)	59.7	57.0
Resin (%)	38.1	43.0
Voids (%)	2.2	0.1
Densities		
Fiber ρ_F (gm/cc)	1.74	1.74
Matrix ρ_M (gm/cc)	1.21	1.21
Composite ρ_c (gm/cc)	1.50	1.51

[a] Gantrez 169 is a high molecular weight copolymer of maleic anhydride and methyl vinyl ether applied to the fiber tow and a 1% (by weight) solution in methyl ethyl ketone solvent and dried on the fiber surface.

[b] Graphite HTS fibers heat treated for 120 min at 1038°C in a 90/10 :: hydrogen/nitrogen atmosphere.

axially reinforced composite plates described in Table IV were molded using preimpregnation and curing procedures detailed in an earlier report.[4] The temperature and pressure cycles applied in curing the composites follow resin manufacturer's recommendations which achieve final curing conditions of 177°C for 2 hours.

Previous studies of high moisture aging had shown the standard short beam shear test (ASTM D2344–67) produced combinations of transfibrous (see Figure 1) and interlaminar shear failure.[4] The sample and test geometry shown in the upper view of Figure 2 was developed as a replacement to the short beam shear test. In the compression shear test shown in Figure 2, a composite sample $1.50 \times 0.50 \times 0.50$ cm outer dimensions is cut from the panel with fibers parallel to the sample length. Two 0.50 cm wide by 0.25 cm deep grooves are then cut in the transfibrous direction (see Figure 1) so as to produce an interlaminar shear plane of 0.50×0.50 cm dimensions when the specimen is placed under end compression. The compression shear test is a small scale analog of the side notched tensile test specimen (FTMS 406, method 1042) applied to measure interlaminar shear strength.

Compression shear specimens as shown in Figure 2 were cut from the cured composite panels as described in Table IV. These samples were hydrothermally aged for varied times $t = 0$ to 1000 hours under liquid water immersion at 100°C. Compression shear measurements were conducted at 23°C immediately after the test specimen is removed from the hydrothermal aging environment using an Instron crosshead speed of 0.02 cm/min. Interlaminar shear strength is expressed by the following relation:

$$\lambda_b = F_b/a_0 \tag{18}$$

where F_b = the compressional force at break and $a_0 = 0.25\ \text{cm}^2$ is the nominal cross sectional area of the shear plane. Sample weighing immediately upon removal from hydrothermal aging and subsequent to extended desiccation over anhydrous calcium sulphate permits determination of moisture content at the time of interlaminar shear strength testing.

Subsequent to hydrothermal aging, shear strength and desiccation to determine moisture content, all samples were subject to ultrasonic inspection using through transmission (c-scan) at 2.25 MHz. The ultrasonic apparatus is similar to that described by Tauchert[14] with the sound propagated in the translaminar (x-axis of Figure 1) direction. The 5×5 mm ends of the test specimens are acoustically coupled via thin films of Nonaq grease (Fisher Scientific Co.) to the signal transmission and detector transducers of a Sperry Reflectoscope UM721 (Customation Industries, Inc.). A constant compression force of 8.1 kg is maintained between the transducers to provide reproducible signal transmission. The delay time $\Delta t = t_2 - t_1$ and signal amplitude ratio A_2/A_1 are measured where t_1, t_2 and A_1, A_2 are the respective signal arrival times (μsec) and amplitude (volts) without sample (subscript 1) and with

sample (subscript 2) of thickness $L = 0.50$ cm. The longitudinal sound velocity C_L (km/sec) and nominal acoustic absorption coefficient α_L (nepers/cm) are evaluated from the following standard relations:

$$C_L = L/\Delta t = L/(t_2 - t_1) \tag{19}$$

$$\alpha_L = L^{-1} \ln (A_1/A_2) \tag{20}$$

These nominal values of C_L and α_L response provide a nondestructive test for combined effects of hydrothermal aging, compressive loading to shear failure, and subsequent desiccation on the graphite–epoxy composite.

RESULTS AND DISCUSSION

The analysis for hydrothermal degradations based upon surface energetics considerations, as outlined by the assumptions of Eq. 1 through Eq. 13 is summarized in Table V. Inspection of Eq. 2 through Eq. 5 shows that the

TABLE V

Summary of surface energetics analysis

Composite	SC-2-2[a]	SC-2-3	Units	Equation
α_1	6.10	6.10	$(\text{dyn/cm})^{\frac{1}{2}}$	
β_1	2.88	2.88	$(\text{dyn/cm})^{\frac{1}{2}}$	
α_3	4.67	6.23	$(\text{dyn/cm})^{\frac{1}{2}}$	
β_3	7.14	3.58	$(\text{dyn/cm})^{\frac{1}{2}}$	
R_0	2.25	0.40	$(\text{dyn/cm})^{\frac{1}{2}}$	(2)
H	5.39	6.17	$(\text{dyn/cm})^{\frac{1}{2}}$	(4)
K	5.01	3.23	$(\text{dyn/cm})^{\frac{1}{2}}$	(5)
Air immersion ($\alpha_2 = \beta_2 = 0$)				
R (air)	7.36	6.96	$(\text{dyn/cm})^{\frac{1}{2}}$	(3)
$\sigma_c(\pi c/2E)^{\frac{1}{2}}$	7.01	6.95	$(\text{dyn/cm})^{\frac{1}{2}}$	(6)
Water immersion ($\alpha_2 = 4.67$, $\beta_2 = 7.14$)				
R (H_2O)	2.25	4.19	$(\text{dyn/cm})^{\frac{1}{2}}$	(3)
$\sigma_c(\pi c/2E)^{\frac{1}{2}}$	0	4.17	$(\text{dyn/cm})^{\frac{1}{2}}$	(6)
Degradation factors ($V \simeq 0.60$)				
f_I	0.87	0.87		(8)
$r = \lambda_{b\infty}/\lambda_{b0}$	0.13	0.65		(13)

[a] Calculation assumes hydrated fiber surface with α_3, β_3 values characteristic of bulk water.

modified Griffith fracture criteria of Eq. 1 can be conveniently represented on a graph of α versus β as shown in Figure 3. The left view of Figure 3 shows the location of the α versus β points for the matrix and fiber surfaces of composite SC-2-2. The right view of Figure 3 presents the α versus β

points for composite SC–2–3. The vectors R (air) and R (H_2O) originate at H, K as defined by Eq. 4 and Eq. 5 and terminate at $\alpha = \beta = 0$ for air immersion and $\alpha = 4.67$ (dyn/cm)$^{-\frac{1}{2}}$ and $\beta = 7.14$ (dyn/cm)$^{\frac{1}{2}}$ for water immersion. The R_0 vectors of Figure 3 also originate at H, K and describe a circle which encloses the region where $R \leqslant R_0$ and from Eq. 6 it is predicted that $\sigma_c = 0$.

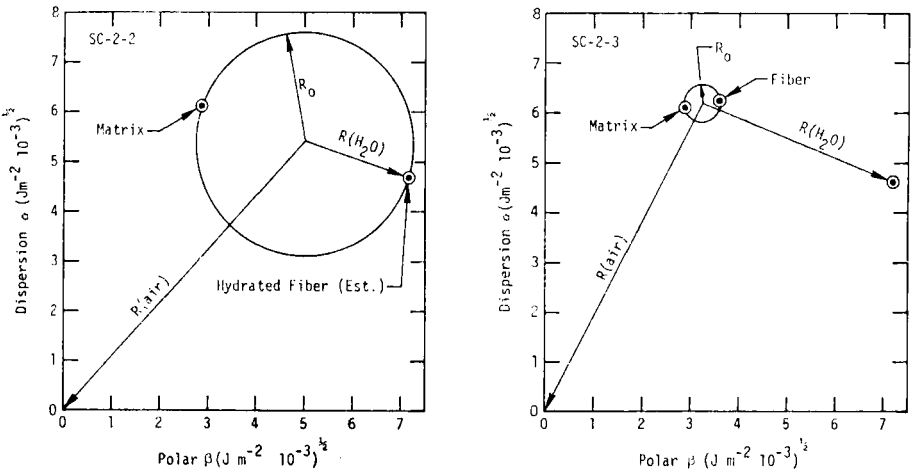

FIGURE 3 Surface energy analysis for fiber-matrix interactions for composite SC–2–2 (left view) and SC–2–3 (right view).

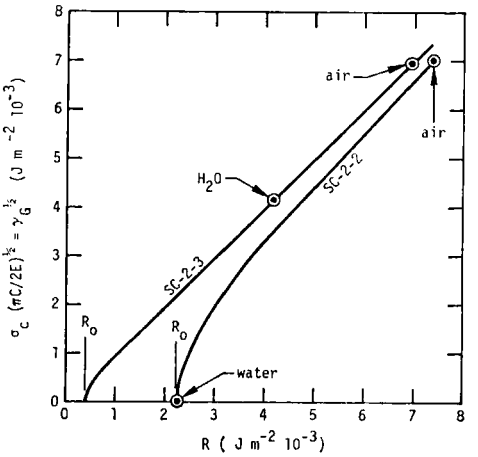

FIGURE 4 Griffith failure criteria $\sigma_c \propto \gamma_G^{\frac{1}{2}}$ for composite SC–2–3 and SC–2–3.

The master functions of $\sigma_c(\pi c/2E)^{\frac{1}{2}} = \gamma_G^{\frac{1}{2}}$ versus R presented in Figure 4 show air and water immersion environments as two special cases. For constant values of $(\pi C/2E)$ the curves of Figure 4 show $\sigma_C(H_2O)/\sigma_c(\text{air}) = 0$ for SC–2–2 and $\sigma_c(H_2O)/\sigma_c(\text{air}) = 0.60$ for SC–2–3. Assuming that interlaminar shear failure involves a combination of interfacial and bulk matrix as described by Figure 2 (lower view) and Eq. 13 we arrive at a final prediction based on surface energetics that $\lambda_{b\infty}/\lambda_{b0} = 0.13$ for SC–2–2 and $\lambda_{b\infty}/\lambda_{b0} = 0.65$ for SC–2–3 where λ_{b0} and $\lambda_{b\infty}$ refer to interlaminar shear strengths for respective hydrothermal aging times $t = 0$ and $t = \infty$.

Inspection of composite fracture surfaces produced by interlaminar shear testing provides confirmation that the locus of failure follows the contour shown in Figure 2 (lower view) where a combination of fiber and matrix surface will be exposed. A high magnification (4000×) scanning electron microscope (SEM) view of a single HTS graphite fiber surface is shown in Figure 5 where the longitudinal surface situations and essentially circular cross section are characteristic of the polyacrylonitrile (PAN) precursor material.

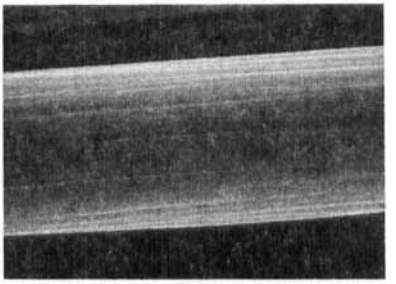

FIGURE 5 SEM view (4000×) of virgin Hercules HTS-S® graphite fiber with diameter $d \simeq 10\ \mu$m showing longitudinal surface striations.

The SEM views of Figure 6 shows the fracture surfaces from interlaminar shear testing of SC–2–2 (left view) and SC–2–3 (right view) before hydrothermal aging where $t = 0$. The fracture surface of SC–2–2 (left view) displays numerous circular features associated with the 2.2% internal voids (see Table IV) present in this composite material. These same circular features are not displayed in the fracture surface of unaged SC–2–3 where internal void content is $\leqslant 0.1\%$. These internal voids are, of course, produced during fabrication and curing and due to the rigidity of the matrix phase, do not change size or shape during hydrothermal aging. The fracture surfaces of Figure 6 also show that the fiber orientations and spacings are somewhat nonuniform. The 100 μm bench marks in Figure 6 indicate the local scale of void structure and interfiber distance characteristic of the elementary microfracture processes.

The SEM views of Figure 7 show more details of the fracture surfaces from interlaminar shear of unaged (left view) and fully aged (right view) samples of SC–2–2. The 10 μm bench marks below the views of Figure 7 indicate the local scale of micro crack and tearing process evident in the matrix phase of

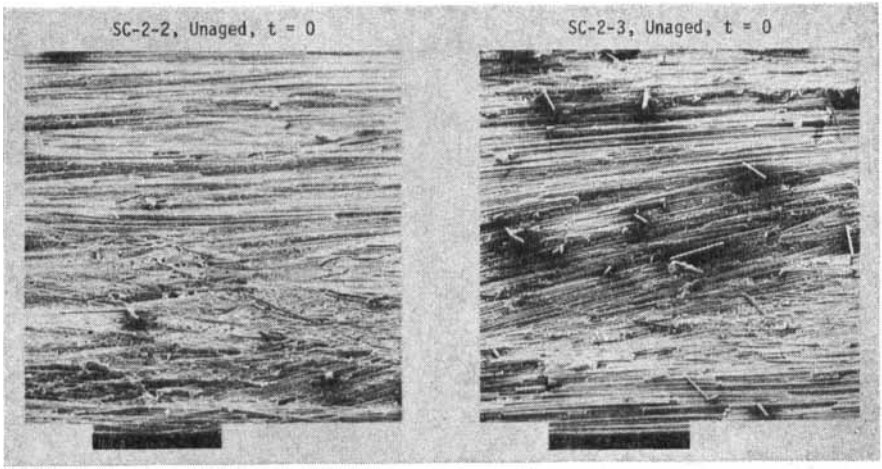

FIGURE 6 SEM views of fracture surfaces for unaged composites SC–2–2 (left) and SC–2–3 (right), note 100 μm benchmarks.

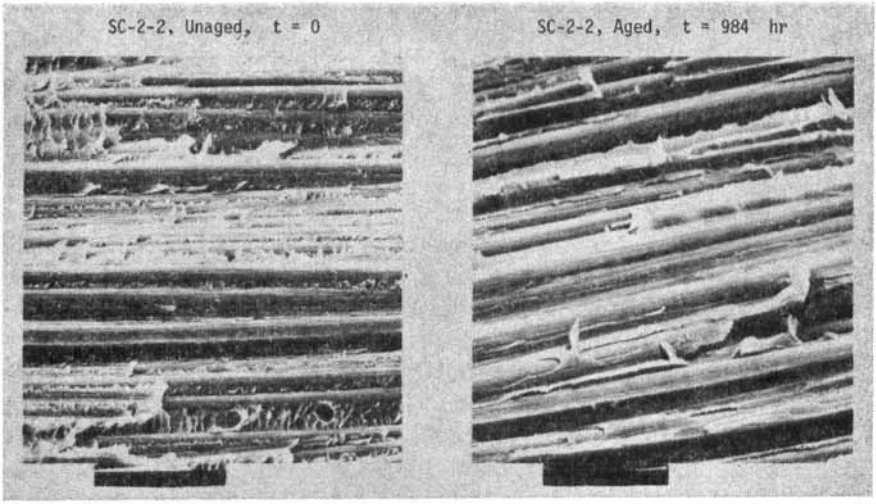

FIGURE 7 SEM views of fracture surfaces for unaged (left view at $t = 0$) and hydrothermally aged (right view at $t-984$ hr) for composite SC–2–2, note 10 μm benchmarks.

both unaged and aged SC–2–2 composite. The exposure of the striated surface of the graphite fiber in both the left and right views of Figure 7 confirms that fiber-matrix interface failure occurs in both unaged and aged specimens of SC–2–2. Inspection of other fracture surfaces with intermediate degrees of hydrothermal aging confirm that the locus is generally described by the schematic of lower Figure 2.

The SEM views of Figure 8 present typical fracture surfaces from interlaminar shear of unaged (left view) and hydrothermally aged (right view) samples of SC–2–3 composite. In both views the well defined fiber surfaces indicate the primary locus of fracture is at the fiber-matrix interface for the

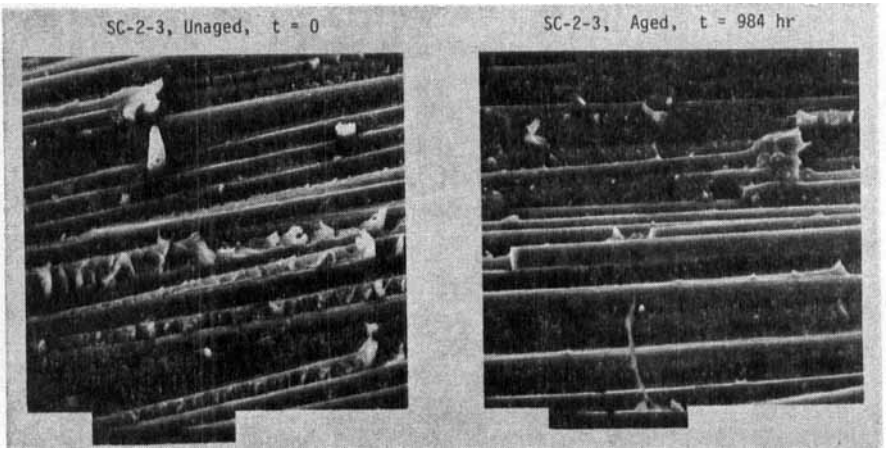

FIGURE 8 SEM views of fracture surfaces for unaged (left view at $t = 0$ hr) and hydrothermally aged (right view at $t = 984$ hr) for composite SC–2–3, note 10 μm benchmarks.

whole range of hydrothermal aging conditions. The SEM views of Figure 7 and Figure 8 illustrate that the locus of failure remains at the fiber-matrix interface for varied conditions of hydrothermal aging. These micrographs also show that the unaged composites display more extensive microcrack structure in the matrix which intervenes adjacent reinforcing fibers indicative of higher stresses for crack propagation.

The experimental measurements of hydrothermal aging under H_2O immersion at 100°C on interlaminar shear strength λ_b, moisture content ($\%H_2O$), and ultrasonic response Δt and A_2 of the subsequently desiccated specimens are summarized in Table VI for SC–2–2 and Table VII for SC–2–3. Averaged values of λ_b and wt. $\%$ H_2O are plotted versus hydrothermal aging time t in Figure 9. The curves of Figure 9 show the dramatic effect that the moisture sensitization of SC–2–2 composite has in diminishing interlaminar

shear strength λ_b (upper curves) and increasing wt. % H_2O (lower curves) with increased hydrothermal aging time t.

Inspection of Table VI and Table VII as the graphs of Figure 8 show that interlaminar shear strength λ_b apparently varies with hydrothermal aging time t according to the kinetic model summarized by Eq. 16 or Eq. 17. A summary of the kinetics of degradation for interlaminar shear strength λ_b

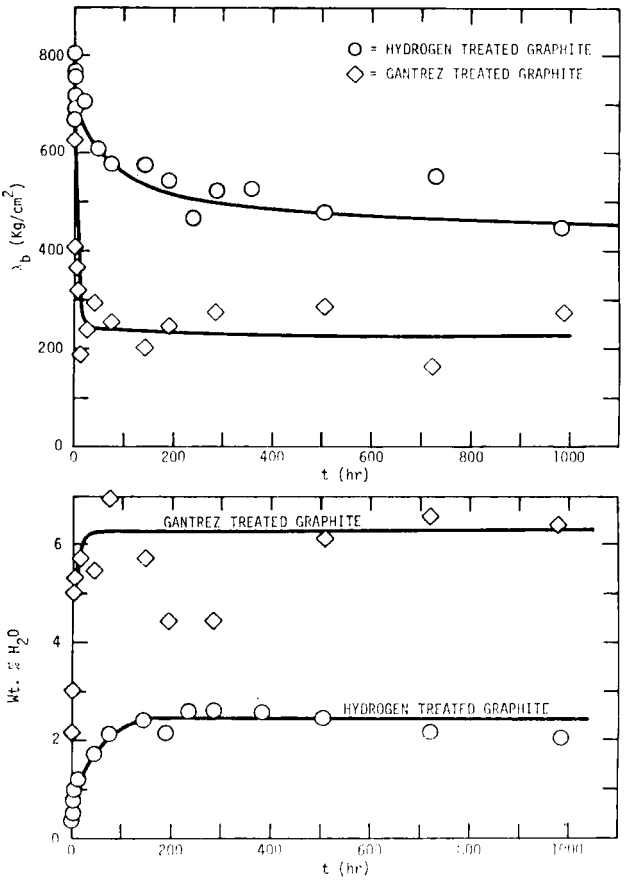

FIGURE 9 Dependence of interlaminar shear strength λ_b (upper view) and moisture content as Wt. % H_2O (lower view) on hydrothermal aging time t at 100°C in H_2O.

with hydrothermal aging time t is presented in Table VIII. In this analysis Eq. 16 is applied to define the coefficients of the average and extreme value (+) or (−) functions that enclose all the λ_b data of Table VI and Table VII respectively. The kinetic analysis of Table VIII shows that both composite materials achieve equilibrium degrees of degradation, where $\phi = 0$ in Eq. 15.

The extent of equilibrium hydrothermal degradation $r = \lambda_{b\infty}/\lambda_{b0} = 0.13$ predicted (see Table V) for SC–2–2 is lower than the experimentally determined range $r = 0.37 \pm 0.11$ (see Table VIII) probably due to the extreme assumption that Gantrez sized fiber displays the surface properties of bulk water. A good agreement between predicted values of $r = 0.65$ (see Table V)

TABLE VI

Hydrothermal (100°C in H_2O) aging effects on composite SC–2–2

t (hour)	λ_b (kg/cm²)	Wt. % H_2O	C_L (km/sec)	α_L (neper/cm)
0	576	0	2.69	4.99
	700	0	2.69	5.88
	592	0	2.70	5.48
1	388	1.97	2.66	7.95
	424	2.35	2.58	8.36
2	472	3.08	2.67	8.29
	260	2.98	2.42	9.21
5	280	5.30	2.30	12.31
	346	4.68	2.30	11.04
8	332	5.31	2.29	12.68
	398	5.29	2.25	12.49
13	184	5.71	2.15	11.91
21	283	—		
	194	—		
46	323	4.58		
	242	6.51		
71	240	7.06		
	268	6.82		
143	182	6.78		
	222	4.67		
190	234	5.01	$A_2 \leqslant 0.030$ Volts	
	260	3.86		
285	234	5.31		
	306	3.59		
505	294	6.24		
	278	6.02		
720	179	6.64		
	149	6.53		
984	224	6.52		
	328	6.28		

Sample dimensions $Z = 4 = X = 0.50$ cm, sound propagated along X axis (see Figure 1) with $L = 0.50$ cm and $A_1 = 17.0$ volts.

and experimental range values of $r = 0.67 \pm 0.09$ (see Table VIII) for SC–2–3 probably reflects the more accurate description of fiber surface properties α_3, β_3 for this composite material. The scatter in interlaminar shear data shown in Table VI and Table VII is typical of composite response and reflects

the real heterogeniety of microstructure revealed by the fracture surfaces of Figure 6 through Figure 8.

Inspection of Table VI and Table VII or the curves of Figure 9 points out the close apparent correlation between the kinetics of shear strength degradation and water absorption in composites SC–2–2 and SC–2–3. Earlier studies[4] on related graphite–epoxy composites had demonstrated similar correlations between kinetics of strength degradation and water absorption for both water vapor (100% R.H.) and water immersion aging.

TABLE VII

Hydrothermal (100°C in H_2O) aging effects on composite SC–2–3

t K	λ_b kg/cm²	Wt. % H_2O	C_L (km/sec)	α_L (neper/cm)
0	760	0	2.92	5.92
	656	0	3.01	6.11
	652	0	2.98	5.14
1	672	0.35	—	—
	664	0.37	—	—
2	764	0.42	—	—
	764	0.52	2.82	6.02
5	756	0.82	2.82	4.99
	856	0.78	—	—
8	696	1.03	2.81	6.38
	736	0.95	2.82	5.97
13	768	1.19	2.82	6.11
21	700	—	2.81	7.50
	704	—	2.81	7.50
46	628	1.80	2.78	6.44
	584	1.62	2.82	6.56
71	464	2.01	2.72	7.22
	692	2.31	2.69	8.79
143	576	2.20	2.67	8.52
	572	2.60	2.60	8.79
190	488	2.49	2.62	9.21
	604	1.88	2.24	10.85
237	436	2.63	2.51	12.43
	496	2.63	—	—
285	576	2.65	2.56	10.98
	469	2.64	2.07	12.01
357	628	2.34	2.53	13.30
	426	2.86	—	—
505	378	2.49	2.67	13.04
	574	2.44	2.67	12.31
720	652	2.32	2.63	13.04
	450	2.26	2.69	9.83
984	456	2.00	2.70	14.35
	440	2.09	2.67	12.01

Same measurement geometry as Table VI.

This earlier study had also shown that the current moisture content of a composite material is not a necessary index of prior hydrothermal degradation of interface strength. Hydrothermal degradation of the bonded interface between the cured epoxy matrix and graphite reinforcement can be reasonably considered to be substantially irreversible. The original fiber-matrix bonding occurs prior to curing when the resin is in a simple liquid state whereas rebonding subsequent to curing is, of course, restricted by the limited molecular motion of the highly crosslinked epoxy.

TABLE VIII

Kinetics of hydrothermal degradation in interlaminar shear strength
$\lambda_b(t) = \lambda_{b\infty} + (\lambda_{b0} - \lambda_{b\infty}) \exp(-t/\gamma)$

Composite	λ_{b0} (kg/cm²)	$\lambda_{b\infty}$ (kg/cm²)	$\lambda_{b0} - \lambda_{b\infty}$) (kg/cm²)	γ (hour)	$\lambda_{b\infty}/\lambda_{b0}$
SC-2-2	700	328	372	4.82	0.47
	576	149	427	1.48	0.26
average	638	238	400	3.15	0.37
max. dev.	±62	±90	±27	±1.67	±0.11
SC-2-3	856	652	204	43.6	0.76
	652	378	274	61.3	0.58
average	754	515	239	52.5	0.67
max. dev.	±102	±137	±35	±8.9	±0.09

The combined effects of hydrothermal aging and subsequent desiccation to zero moisture content produce irreversible changes in the acoustic properties. The right hand data columns of Table VI and Table VII summarize the measured values of sound velocity C_1 and attenuation α_L for SC-2-2 (moisture sensitive) and SC-2-3 (moisture stabilized) composites respectively. The data plots and dashed standard deviation curves in Figure 10 show that the general effect of lowering λ_b due to hydrothermal aging of both composites is to decrease sound velocity C_L and increase acoustic attenuation α_L. The data scatter evident in Figure 10 is probably due in part to the intrinsic micro heterogeniety which influences λ_b. A second important scatter factor is reflected in the fact that λ_b is determined by the local microstructure in the plane of failure while both C_L and α_L are volume averaged properties over the 0.50 cm sample thickness. Inspection of Table VI and Table VII shows that ultrasonic inspection of desiccated specimens provides direct information of the effects of prior hydrothermal aging history and evidence of the irreversible changes induced in physical state of the composite material.

A special experiment was carried out on composite SC-2-2 (moisture sensitive) where measurements of C_L and α_L were applied to track the

dynamic effects of hydrothermal aging. The data summary in Table IX shows that ultrasonic measurements are highly sensitive to cumulative hydrothermal aging time (t). The acoustic property changes shown in Table IX for a hydrated composite parallels the trends shown for desiccated samples of hydrothermal aged specimens shown previously in Table VI for composite SC–2–2.

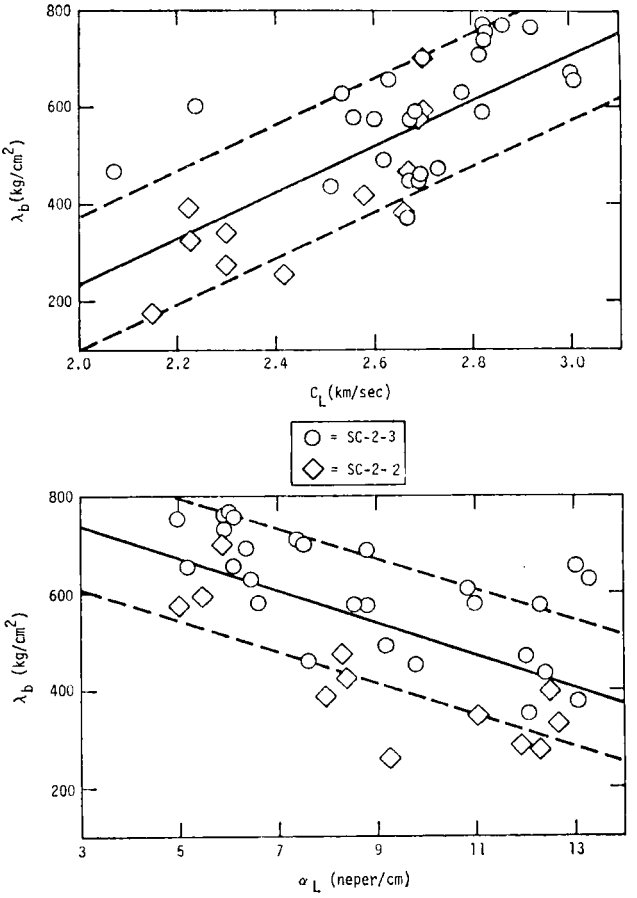

FIGURE 10 Variation of hydrated interlaminar shear strength λ_b with desiccated sound velocity C_L (upper view) and attenuation α_L (lower view) for composites SC–2–2 and SC–2–3.

A final experiment was carried out on composite SC–2–3 (moisture resistant) to determine the impact of prior hydrothermal aging (1000 hr. in H_2O at 100°C) and subsequent full desiccation (at 23°C) upon the temperature dependence of interlaminar shear strength λ_b. The temperature

TABLE IX

Effect of hydrothermal aging (100°C in H_2O) on the ultrasonic response of SC-2-2 composite tested at 2.25 MHz at 23°C in the hydrated state

Aging time (t) t (min)	C_L (km/sec)	α_L (neper/cm)
0	2.92	3.16
2	2.86	3.92
6	2.81	5.30
10	2.79	4.73
23	2.76	6.44
37	2.70	8.07
≃1440 (24 hr)	2.55	9.46

Sample dimensions $Z = 1.50$ cm, $y = 1.29$ cm, $x = 0.50$ cm, sound propagated along X axis (see Figure 1) with $L = 0.50$ cm and $A_1 = 17.0$ volts.

TABLE X

Prior hydrothermal aging (100°C in H_2O) effects on the temperature dependence of interlaminar shear strength of desiccated composite SC-2-3

Unaged ($t = 0$) T (°C)	λ_b (kg/cm²)	Aged ($t = 1000$ hr) T (°C)	λ_b (kg/cm²)
−87	1000	−80	760
	820		800
−67	850		880
	860	−40	460
−42	860		960
	840		940
0	880	−20	500
	875		620
25	760	3	608
	740		592
51	580	25	480
	740		496
	740	54	580
75	660		448
	560	83	296
100	420		240
	440	100	140
110	240		170
	340		
125	70		
	80		

dependence of λ_b for unaged composite in fully desiccated condition was also determined for this composite and the experimental data are summarized in Table X and averaged values of λ_b versus test temperature in Figure 11. The separation of the two curves of Figure 11 indicates the impact of full hydrothermal aging in degrading the function of λ_b versus T for composite SC–2–3. At 25°C the data of Table X and Figure 11 show that $\lambda_{b0} \simeq 750$ kg/cm^2 and $\lambda_{b0} \simeq 485$ kg/cm^2 with $\lambda_{b0} - \lambda_{b\infty} \simeq 265$ kg/cm and $\lambda_{b\infty}/\lambda_{b0} \simeq 0.65$ which correlates with shear strength degradation of hydrated test specimens summarized for SC–2–3 in Table VIII.

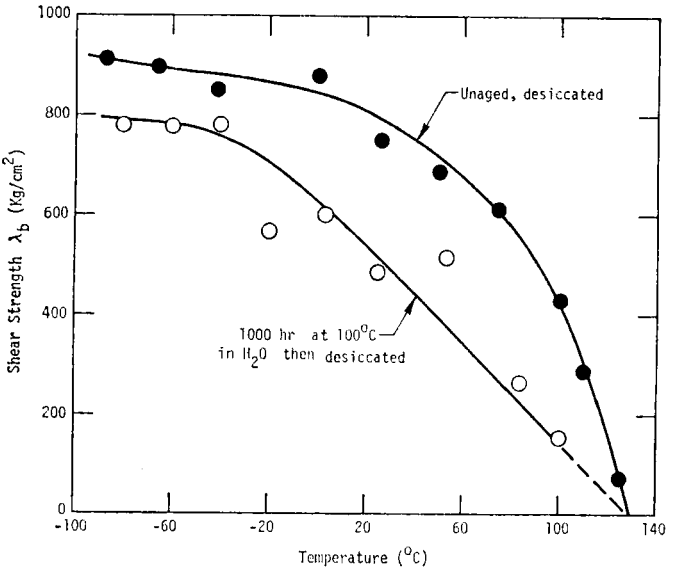

FIGURE 11 Temperature dependence of interlaminar shear strength λ_b for unaged ($t = 0$) and hydrothermally aged ($t = 1000$ hr) samples of composite SC–2–3.

Additional features of Figure 11 indicate that λ_b *versus* T extrapolates to $\lambda_b \simeq 0$ at $T \simeq 130$°C for both unaged and aged composites. This zero shear strength condition coincides with the glass (alpha) transition temperature T_g of the cured epoxy matrix.[15] At temperatures below $T_\beta = -60$°C, which coincides with the characteristic secondary (beta) transition in glycidyl ether epoxy resins, the curves of Figure 11 show that λ_b values plateau to become essentially temperature independent. Over the broad range of potential use temperature from $T = -60$ to 100°C, it is evident in Figure 11 that hydrothermal aging of SC–2–3 modifies the temperature dependence of λ_b which implies that the matrix rheological response is also modified by hydrothermal aging.

The combined effects of prior hydrothermal aging (at 100°C in H_2O) time t

and current test temperature T on interlaminar shear strength λ_b of composite SC–2–3 are shown schematically in Figure 12. The two experimental curves of Figure 11 from the left ($t = 0$) and right ($t = 1000$ hr) edges of the λ_b response surface of Figure 12. The hydrothermal degradation curves at constant T shown in Figure 12 are developed from the kinetic coefficients summarized in Table VIII for composite SC–2–3. A general definition of interlaminar shear strength is shown by Figure 12 to combine a model for interface degradation which defines λ_b versus t with an additional considera-

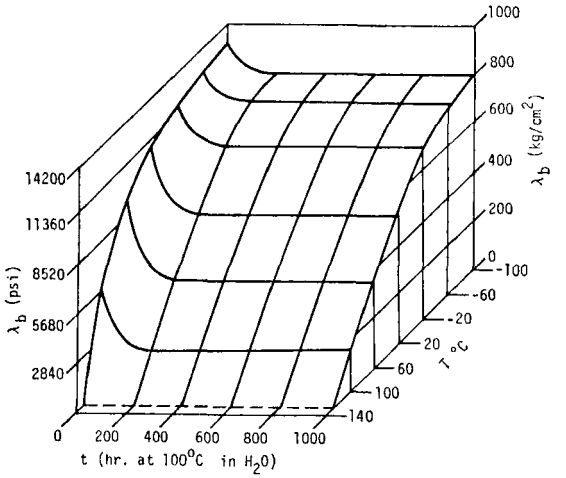

FIGURE 12 Response surface of interlaminar shear strength for composite SC–2–3 versus prior hydrothermal aging time (t) and current test temperature (T).

tion of matrix rheology and physical state which dominantly determines λ_b versus T. It thus becomes evident that the progressive effects of hydrothermal aging on the graphite–epoxy composite appear to involve measureable and independent shifts in both interface and bulk (matrix) properties as measured nondestructively by ultrasonic inspection or destructive by interlaminar shear strength testing.

SUMMARY AND CONCLUSIONS

This report summarizes a study in which selected surface treatments were applied to graphite fiber to produce both sensitization and stabilization to hydrothermal aging of the graphite–epoxy composite. The study shows that significant differences in both the kinetics and extent of hydrothermal degradation result (see Table VIII). These results provide further experimental confirmation of recently proposed interfacial protection mechanisms

for moisture stabilization of fiber reinforced composite materials.[4, 10] The degradation of interlaminar shear strength λ_b by hydrothermal aging is shown to be essentially irreversible and to degrade the function of λ_b versus T over a broad temperature range from $T = -90°C$ to 100°C.

Ultrasonic (2.25 MHz) measurements, transverse to the fiber reinforcement, shows that hydrothermal aging of both moisture sensitized (SC–2–2) and stabilized (SC–2–3) composites produces systematic decreases in sound velocity C_L and increased attenuation α_L which correlates with the kinetics of degradation in interlaminar shear strength λ_b. These results are shown for both hydrated composite and desiccated composite subject to prior hydrothermal aging. This study reinforces and extends an earlier observation[4] that ultrasonic measurements provide an effective nondestructive evaluation (NDE) tool for effects of prior hydrothermal degradation. The combined decrease in C_L and increase in α_L indicates a changed physical response state in the composite material which is also evidenced in the modified temperature dependence of λ_b.

Further studies are required to provide a more detailed basis for developing a physical model for correlations between volumetric properties, as measured by acoustic responses such as C_L and α_L, and critical two dimensional properties at the locus of fracture. A more detailed study of the rheological and physical state aspects of hydrothermal aging in the above composite materials has been undertaken. This phase of study forms part II of this report and develops the important and semi-independent contribution to composite response and hydrothermal sensitivity provided by the epoxy matrix phase. The present analysis has emphasized the interfacial degradation process as related to surface energetics (see Theory). The response surface of interlaminar shear strength λ_b versus both prior hydrothermal aging time t and current test temperature T shown in Figure 11 emphasizes the importance of interface and bulk (matrix) properties of the reinforced composite materials.

Acknowledgement

This research was sponsored by the Center for Advanced NDE operated by the Science Center, Rockwell International for the Advanced Research Projects Agency and the Air Force Materials Laboratory under Contract F33615–74–C–5180. Materials selection, fabrication, and preliminary characterization was provided for by the Rockwell International IR&D Interdivisional Technology Program.

References

1. D. H. Kaelble, *Proc. 23rd Int. Cong. on Pure and Appl. Chem.*, Vol. 8 (Butterworths, London, 1971). Pp. 265–302.
2. D. H. Kaelble, *J. Adhesion* **5**, 245 (1973).
3. D. H. Kaelble, *ibid.* **6**, 23 (1974).

4. D. H. Kaelble, R. J. Dynes, L. H. Crane and L. Maus, *ibid.* **7,** 25 (1974).
5. B. Harris, P. W. R. Beaumont and E. M. deFerran, *J. Matl. Sci.* **6,** 238 (1971).
6. P. W. R. Beaumont and B. Harris, *J. Comp. Matls.* **7,** 1265 (1972).
7. E. L. McKague, Jr., J. E. Halkias and J. D. Reynolds, *J. Comp. Matls.* **9,** (1975).
8. W. G. Cook and A. G. Downhill, *Carbon Fibers in Engineering*, M. Langley, Ed. (McGraw-Hill, Maidenhead, 1973). Chapter 7.
9. P. J. Dynes and D. H. Kaelble, *J. Adhesion* **6,** 195 (1974).
10. D. H. Kaelble, P. J. Dynes and L. Maus, *ibid.* **6,** 239 (1974).
11. D. H. Kaelble, *J. Appl. Poly. Sci.* **18,** 1869 (1974).
12. J. C. Halpin and H. W. Polley, *J. Comp. Matls.* **1,** 64 (1967).
13. J. C. Halpin, *ibid.* **6,** 208 (1972).
14. T. R. Tauchert, *J. Comp. Matls.* **8,** 195 (1974).
15. D. H. Kaelble, in *Epoxy Resins*, C. A. May and Y. Tanaka, Eds. (Dekker, New York, 1973). Chapter 5.